

Robust Output-feedback Predictive Control for Proximity Eddy Current De-tumbling with Constraints and Uncertainty

Xiyao Liu, Student Member, IEEE
Northwestern Polytechnical University, Xi'an, China

Haitao Chang, Member, IEEE
Northwestern Polytechnical University, Xi'an, China

Panfeng Huang, Senior Member, IEEE
Northwestern Polytechnical University, Xi'an, China

Zhenyu Lu
Bristol Robotics Laboratory & University of the West of England,
Bristol, UK

Abstract— Proximity operation can significantly improve the efficiency of eddy current de-tumbling. However, the tumbling motion and non-cooperation of space debris make the chaser execute collision avoidance maneuvers and be influenced by model uncertainty. In this paper, an inertial-oriented safety corridor is proposed by taking the debris' angular momentum as the central axis, which can avoid the frequent collision maneuvers of the chaser. Meanwhile, a desired de-tumbling trajectory under this safety corridor is designed to de-tumble the angular velocity of space debris. Then, a robust output-feedback controller considering safety corridor and model uncertainty is proposed by combining moving horizon estimation and model predictive control. The moving horizon estimation is employed to estimate the system state and model uncertainty which is compensated by a feedforward control law. Furthermore, the model predictive control without terminal ingredients is designed to realize the optimal performance of fuel consumption and the robust tracking stability of the system. Finally, taking the Chinese Sinosat-2 satellite as the simulation case, the effectiveness of the proposed scheme is verified.

Manuscript received XXXXX 00, 0000; revised XXXXX 00, 0000; accepted XXXXX 00, 0000.

This research was supported by the National Natural Science Foundation of China (Grant No. 61725303 and No. 62103337). (Corresponding author: Haitao Chang).

Xiyao Liu, Haitao Chang, and Panfeng Huang are with the Research Center for Intelligent Robotics, School of Astronautics, Northwestern Polytechnical University, Xi'an 710072, China, and also with the National Key Laboratory of Aerospace Flight Dynamics, Northwestern Polytechnical University, Xi'an 710072, China (e-mail: liuxiyao@mail.nwpu.edu.cn, htchang@nwpu.edu.cn, pffuang@nwpu.edu.cn). Zhenyu Lu is with Bristol Robotics Laboratory & University of the West of England, Bristol, UK (e-mail: Zhenyu.lu@uwe.ac.uk).

0018-9251 © 2022 IEEE

Index Terms— Eddy current de-tumbling, Safety corridor, Output-feedback control, Moving horizon estimation, Model predictive control

I. INTRODUCTION

IN the last 60 years, humanity has launched around 12,450 satellites and produced approximately 30,630 pieces of space debris, which the Space Surveillance Networks have constantly monitored [1]. The ever-increasing space debris has been viewed as a severe hazard to future space missions. It is known that the higher the mass of debris, the greater the risk of collision with operational satellites. Large debris, such as defunct satellites and spent rocket bodies, account for more than 90% of the total mass of space debris in orbit [2]. Thus, active removal of these large pieces of debris can substantially minimize the risk of collision in space.

However, unlike operational satellites, space debris often tumbles owing to passivation, collisions, environmental moments, etc. Photometric data [3] show that the defunct satellite with the max angular velocity in geosynchronous orbit (GEO) is INTELSAT 4-F7 (1973-058A). The angular velocity of the satellite is 139.1 ($^{\circ}$ /s). The rocket body with the max angular velocity in GEO is BREEZE-M R/B (2015-075B), while the angular velocity value is 409.6 ($^{\circ}$ /s). This high-speed and even irregular rotation makes it a complex problem to remove space debris actively. Therefore, space debris de-tumbling [4] is proposed to reduce the rotation angular velocity of space debris before capturing.

In the past few decades, scholars have proposed a variety of contact or non-contact de-tumbling methods, including mechanical pulse de-tumbling [5], dual-arm space robot de-tumbling [6], electrostatic de-tumbling [7], plume impingement de-tumbling [8], eddy current de-tumbling [9], and so on. Among them, eddy current de-tumbling has attracted much attention due to its advantages in terms of practicability and sustainability. The fundamental physical principle of eddy current de-tumbling is that when space debris containing conductive components spins in the magnetic field, the induced current is produced on the conductive parts, resulting in the generation of de-tumbling force/torque [10].

Eddy current de-tumbling may be actively accomplished by utilizing a chaser with a magnetic field generator. Kadaba et al. [11] first suggested this scheme in 1995 and investigated the feasibility of generating eddy current by current loop, bar magnet, or U-shaped electromagnet, respectively. To improve the magnetic field strength and shorten the de-tumbling duration, Gómez et al. [12] employed high temperature superconducting (HTS) coil to de-tumble space debris, as shown in Fig. 1. They investigated and confirmed the magnetic tensor theory [12], the design of the navigation and guidance system [10], and the preliminary scheme of the entire machine design [4], making this technique one of the most comprehensive and promising in engineering and

theory. In addition, Gómez et al. [10] mentioned that the de-tumbling efficiency could be significantly improved by adequate relative distance and pointing between the chaser and the debris. Therefore, the control purpose of eddy current de-tumbling is to decrease the relative distance as much as possible and ensure adequate relative pointing. However, the tumbling motion of the debris and the de-tumbling force/torque on the chaser make it challenging.

The tumbling motion of the debris dramatically increases the risk of collision between the chaser and the debris. Designing suitable safety corridors is essential. The primary safety corridor includes cardioid-based surface [13], convexified ellipsoid [14], and circle/rectangular cone [15], [16]. When space debris is tumbling, the above safety corridor will be time-varying, which will lead to the chaser moving continuously around the debris, increasing the complexity of the de-tumbling process and fuel consumption. Therefore, this paper proposes an inertial-oriented safety corridor based on the debris' angular momentum vector, ensuring that the safety corridor and the desired trajectory only need slight changes. The primary methods for the control problem within the safety corridor are artificial potential field [17] and model predictive control (MPC) [18]. The eddy current de-tumbling often lasts at least several hours. Thus, fuel consumption is an essential index in designing the de-tumbling controller. Naturally, MPC is more suitable for eddy current de-tumbling.

The de-tumbling force/torque, often unknown due to the non-cooperation of debris, leads to the uncertainty of the system dynamics model. It is necessary to develop a robust output-feedback controller for the non-availability of velocity-level information and control input saturation. An estimator for feedback control is a feasible scheme, e.g., output model predictive control [19]. The main estimators include iterative identification estimation [20], Kalman filter [21], moving horizon estimation (MHE) [22], and so on. Due to the safety corridor in the de-tumbling process, the estimated state that exceeds the safety corridor may cause the model predictive control to be infeasible. Considered the infeasible problem and the requirement for estimation accuracy, moving horizon estimation, a constrained optimal estimator which obtains the estimated state by solving a constrained optimization problem is appropriate for the de-tumbling.

Motivated by the above discussion, this paper proposes a robust output-feedback predictive control scheme for proximity eddy current de-tumbling with safety corridor constraint, control input constraint, and uncertainty of de-tumbling force/torque. Unlike the previous study [18], this paper focuses on inertial-oriented safety corridor, model uncertainty, and robust output-feedback tracking control. To the best of our knowledge, these issues have not been studied in eddy current de-tumbling. Further, the innovations of this paper are:

- 1) A novel inertial-oriented safety corridor is presented for the proximity operations of de-tumbling.

Compared with the maximum safe distance de-tumbling in [10] and other usual safety corridors such as [13], [14], [15], [16], [18], the presented safety corridor can reduce the maneuvering frequency of the chaser and improve the de-tumbling efficiency by shortening the relative distance;

- 2) A joint moving horizon estimation (jMHE) is developed to optimally estimate the system state and de-tumbling force/torque simultaneously. Unlike the Extended Kalman Filter (EKF) [21], Unscented Kalman Filter (UKF) [23], and Square-Root Unscented Kalman Filter (SR-UKF) [24], the proposed estimator not only provides stability and high accuracy of the estimated value, but also avoids the over limit of the estimated value and the nonpositive definite of the covariance;
- 3) A robust output-feedback controller combining jMHE and robust tracking model predictive control (RMPC) is designed for de-tumbling space debris with model uncertainty. Compared with other model predictive control schemes, such as [21], [16], [18], [25], the proposed scheme does not need velocity-level information, and ensures the system's robust stability and constraints satisfaction under time-varying model uncertainty.

The remainder of this paper is arranged as follows. Section II defines the reference frames and the relative translational and rotational dynamics of the eddy current de-tumbling. Section III depicts the inertial-oriented safety corridor design procedure and the desired trajectory. The moving horizon estimation and feedforward control low utilized in this paper are presented in Section IV. Section V elaborates on the robust tracking model predictive control, including parameter design and system stability. Section VI presents numerical simulation results applying the designed controller to de-tumble the Chinese Sinosat-2 satellite. At last, Section VII summarizes the paper.

II. Dynamics Model

This paper employs a chaser with HTS coil to de-tumble the space debris (also called 'target'), similar to the scenario mentioned in [12]. There are four reference frames involved in this scenario, shown in Fig.1. The Earth-centered inertial (ECI) reference frame $\mathcal{N} = \{O, \hat{n}_x, \hat{n}_y, \hat{n}_z\}$ is located at the center of Earth, \hat{n}_x points toward the vernal equinox, \hat{n}_z is aligned with the North Pole, and \hat{n}_y completes the triad. The body reference frame of chaser $\mathcal{B} = \{O_b, \hat{b}_x, \hat{b}_y, \hat{b}_z\}$ with its origin is located at the mass center of the chaser. \hat{b}_y is aligned with the coil's magnetic moment m_{Bc} as shown in (9); \hat{b}_x and \hat{b}_z are vertical with \hat{b}_y and complete the triad. The body reference frame of debris $\mathcal{T} = \{O_o, \hat{t}_x, \hat{t}_y, \hat{t}_z\}$ is fixed at the mass center of the debris. \hat{t}_x , \hat{t}_y and \hat{t}_z are aligned with the principal body axes of the debris [26]. The desired reference frame $\mathcal{D} = \{O_b, \hat{d}_x, \hat{d}_y, \hat{d}_z\}$

is located at the mass center of the chaser, and the basic vectors $[\hat{d}_x, \hat{d}_y, \hat{d}_z]$ of frame \mathcal{D} are given by (23) and (25). Furthermore, for any given vector \mathbf{X} , $\mathbf{X}^{\mathcal{N}}$ indicates that \mathbf{X} is written in \mathcal{N} frame; \mathcal{B} , \mathcal{T} , and \mathcal{D} frames are the same.

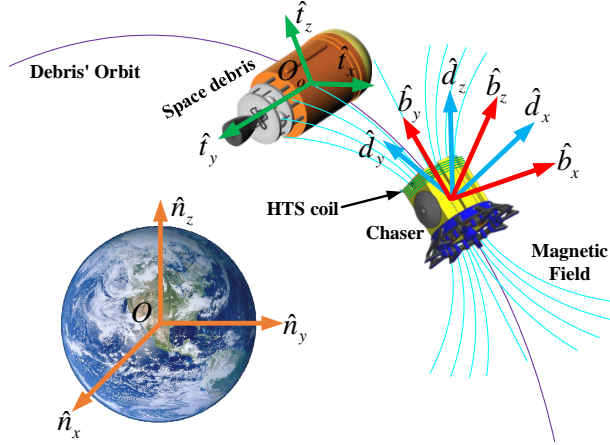


Fig. 1: Definitions of reference frames¹.

A. Relative translational dynamics

The first step to establishing the relative translational dynamics of the de-tumbling problem is to determine the reference frame. The reference frame commonly used to establish the relative translational dynamics of spacecraft include the Local-Vertical-Local-Horizontal (LVLH) frame [28], the line-of-sight (LOS) frame [29], the chaser's body frame [30] and the target's body frame [17]. However, the electromagnetic model is not straightforward in these frames [10], and the safety corridor designed in the following content is fixed in the \mathcal{N} frame. For this reason, the relative translational dynamics is expressed in the \mathcal{N} frame as follows:

$$\ddot{\mathbf{R}}^{\mathcal{N}} = -\frac{G_M}{\|\mathbf{R}^{\mathcal{N}}\|^3} \mathbf{R}^{\mathcal{N}}, \quad (1)$$

$$\ddot{\mathbf{r}}^{\mathcal{N}} = -\frac{G_M}{\|\mathbf{R}^{\mathcal{N}}\|^3} \mathbf{P}_R \mathbf{r}^{\mathcal{N}} + \frac{\mathbf{F}_{Bt}^{\mathcal{N}}}{m_{red}} - \frac{\mathbf{F}_c^{\mathcal{N}}}{m_c}, \quad (2)$$

where $\mathbf{R}^{\mathcal{N}} = \frac{m_t \mathbf{r}_t^{\mathcal{N}} + m_c \mathbf{r}_c^{\mathcal{N}}}{m_c + m_t}$ is the position vector of the chaser-target system centroid, m_c and m_t are the mass of the chaser and the target respectively, $m_{red} = \frac{m_t m_c}{m_t + m_c}$ is the reduced mass of the chaser-target system, \mathbf{r}_c and \mathbf{r}_t are the position vector of the chaser and the target respectively, $\mathbf{P}_R = \mathbf{I}_3 - 3\mathbf{u}_R^{\mathcal{N}} (\mathbf{u}_R^{\mathcal{N}})^{\top}$, $\mathbf{u}_R^{\mathcal{N}} = \frac{\mathbf{R}^{\mathcal{N}}}{\|\mathbf{R}^{\mathcal{N}}\|}$, $\|\mathbf{R}^{\mathcal{N}}\|$ denotes 2-norm for $\mathbf{R}^{\mathcal{N}}$.

In addition, $\mathbf{r}^{\mathcal{N}} = \mathbf{r}_t^{\mathcal{N}} - \mathbf{r}_c^{\mathcal{N}}$ denotes the relative position between the chaser and the target, $G_M = 398,600.44 \text{ (km}^3 \cdot \text{s}^{-2}\text{)}$ represents the standard Earth's gravitational parameter, $\mathbf{F}_{Bt}^{\mathcal{N}}$ is the de-tumbling force given in [18], $\mathbf{F}_c^{\mathcal{N}}$ is the control force.

¹The space debris is shown as a rocket upper stage body, as illustrated in [27].

REMARK 1. To avoid ambiguity, some notations (such as the vector \mathbf{R}) and definitions (such as the chaser-target system) used in this paper are consistent with the 3-D dynamical equations in [10]. Compared with [10], the reference frame of each vector is pointed out.

B. Rotational dynamics

Since the target is tumbling, its attitude changes in a wide range. To avoid attitude singularity, the unit quaternion is used to describe the attitude of the target and the chaser. The rotational dynamics of the target is

$$\dot{\beta}_{t0} = -\frac{1}{2}(\beta_{tv}^{\mathcal{T}})^{\top} \boldsymbol{\omega}_t^{\mathcal{T}}, \dot{\beta}_{tv}^{\mathcal{T}} = \frac{1}{2}((\beta_{tv}^{\mathcal{T}})^{\times} + \beta_{t0} \mathbf{I}_3) \boldsymbol{\omega}_t^{\mathcal{T}}, \quad (3)$$

$$\mathbf{J}_t \dot{\boldsymbol{\omega}}_t^{\mathcal{T}} + \boldsymbol{\omega}_t^{\mathcal{T}} \times \mathbf{J}_t \boldsymbol{\omega}_t^{\mathcal{T}} = \mathbf{T}_{Bt}^{\mathcal{T}}. \quad (4)$$

And the rotational dynamics of the chaser is

$$\dot{\beta}_{c0} = -\frac{1}{2}(\beta_{cv}^{\mathcal{B}})^{\top} \boldsymbol{\omega}_c^{\mathcal{B}}, \dot{\beta}_{cv}^{\mathcal{B}} = \frac{1}{2}((\beta_{cv}^{\mathcal{B}})^{\times} + \beta_{c0} \mathbf{I}_3) \boldsymbol{\omega}_c^{\mathcal{B}}, \quad (5)$$

$$\mathbf{J}_c \dot{\boldsymbol{\omega}}_c^{\mathcal{B}} + \boldsymbol{\omega}_c^{\mathcal{B}} \times \mathbf{J}_c \boldsymbol{\omega}_c^{\mathcal{B}} = \mathbf{T}_c^{\mathcal{B}} + \mathbf{T}_{Bc}^{\mathcal{B}}, \quad (6)$$

where $\beta_t = [\beta_{t0}, (\beta_{tv}^{\mathcal{T}})^{\top}]^{\top}$ and $\beta_c = [\beta_{c0}, (\beta_{cv}^{\mathcal{B}})^{\top}]^{\top}$ are the unit quaternion, $\boldsymbol{\omega}_t^{\mathcal{T}}$ and $\boldsymbol{\omega}_c^{\mathcal{B}}$ are the angular velocity vector, \mathbf{J}_t and \mathbf{J}_c are the inertia tensor of the target and the chaser, respectively. \mathbf{T}_{Bt} denotes the de-tumbling torque on the target, and its expression in frame \mathcal{N} is [10], [12]:

$$\mathbf{T}_{Bt}^{\mathcal{N}} = (\mathbf{M}_{eff}(\boldsymbol{\omega}^{\mathcal{N}} \times \mathbf{B}_{Gt}^{\mathcal{N}})) \times \mathbf{B}_{Gt}^{\mathcal{N}}, \quad (7)$$

in which \mathbf{M}_{eff} is 'Effective Magnetic Tensor' depending on the geometry and conductivity of the target and the inhomogeneity of the magnetic field, and $\boldsymbol{\omega}^{\mathcal{N}} = \boldsymbol{\omega}_t^{\mathcal{N}} - \boldsymbol{\omega}_c^{\mathcal{N}}$ is the relative angular velocity. $\mathbf{B}_{Gt}^{\mathcal{N}}$ is the magnetic field at the center of gravity (COG) of the target described by

$$\mathbf{B}_{Gt}^{\mathcal{N}} = -\frac{\mu_0}{4\pi} \left(\frac{3(\mathbf{m}_{Bc}^{\mathcal{N}} \cdot \mathbf{r}^{\mathcal{N}}) \mathbf{r}^{\mathcal{N}}}{\|\mathbf{r}^{\mathcal{N}}\|^5} - \frac{\mathbf{m}_{Bc}^{\mathcal{N}}}{\|\mathbf{r}^{\mathcal{N}}\|^3} \right), \quad (8)$$

in which $\mu_0 = 4\pi \times 10^{-7} \text{ N} \cdot \text{A}^{-2}$ denotes the permeability of vacuum, $\mathbf{m}_{Bc}^{\mathcal{N}}$ is the magnetic moment of the coil given by

$$\mathbf{m}_{Bc}^{\mathcal{N}} = \pi R_h^2 N_h I_h \hat{\mathbf{b}}_y^{\mathcal{N}}, \quad (9)$$

where R_h is the radius of electromagnetic coil, N_h is the turn of electromagnetic coil, I_h is the electrical intensity, and $\hat{\mathbf{b}}_y^{\mathcal{N}}$ is the y axis base vectors of frame \mathcal{B} expressed in frame \mathcal{N} . In addition, $\mathbf{T}_{Bc}^{\mathcal{N}} = -\mathbf{T}_{Bt}^{\mathcal{N}} - (\mathbf{r}^{\mathcal{N}} \times \mathbf{F}_{Bt}^{\mathcal{N}})$ denotes the de-tumbling torque on the chaser, and $\mathbf{T}_c^{\mathcal{B}}$ is the control torque.

Let $\mathbf{x} = [(\mathbf{r}^{\mathcal{N}})^{\top}, (\dot{\mathbf{r}}^{\mathcal{N}})^{\top}, (\beta_{cv}^{\mathcal{B}})^{\top}, (\boldsymbol{\omega}_c^{\mathcal{B}})^{\top}]^{\top}$, and then the state-space model can be given by

$$\dot{\mathbf{x}} = \mathbf{f}(\mathbf{x}) + \mathbf{B}\mathbf{u} + \mathbf{G}\mathbf{p}, \quad (10)$$

$$\mathbf{y} = \mathbf{C}\mathbf{x}, \quad (11)$$

where

$$\mathbf{f}(\mathbf{x}) = \begin{bmatrix} \dot{\mathbf{r}}^{\mathcal{N}} \\ -\frac{G_M}{\|\mathbf{R}^{\mathcal{N}}\|^3} \mathbf{P}_R \mathbf{r}^{\mathcal{N}} \\ \frac{1}{2}((\beta_{cv}^{\mathcal{B}})^{\times} + \beta_{c0} \mathbf{I}_3) \boldsymbol{\omega}_c^{\mathcal{B}} \\ -\mathbf{J}_c^{-1} \boldsymbol{\omega}_c^{\mathcal{B}} \times \mathbf{J}_c \boldsymbol{\omega}_c^{\mathcal{B}} \end{bmatrix}, \mathbf{B} = \begin{bmatrix} \mathbf{0} & \mathbf{0} \\ -\frac{\mathbf{I}_{3 \times 3}}{m_c} & \mathbf{0} \\ \mathbf{0} & \mathbf{0} \\ \mathbf{0} & \mathbf{J}_c^{-1} \end{bmatrix},$$

$$\mathbf{G} = \begin{bmatrix} \mathbf{0} & \mathbf{0} \\ \mathbf{I}_{3 \times 3}/m_{red} & \mathbf{0} \\ \mathbf{0} & \mathbf{0} \\ \mathbf{0} & \mathbf{J}_c^{-1} \end{bmatrix}, \mathbf{C} = \begin{bmatrix} \mathbf{I}_{3 \times 3} & \mathbf{0} & \mathbf{0} & \mathbf{0} \\ \mathbf{0} & \mathbf{0} & \mathbf{I}_{3 \times 3} & \mathbf{0} \end{bmatrix},$$

$$\text{and } \mathbf{u} = \begin{bmatrix} \mathbf{F}_c^{\mathcal{N}} \\ \mathbf{T}_c^{\mathcal{B}} \end{bmatrix}, \mathbf{p} = \begin{bmatrix} \mathbf{F}_{Bt}^{\mathcal{N}} \\ \mathbf{T}_{Bc}^{\mathcal{B}} \end{bmatrix}.$$

III. Safety corridor and desired trajectory

For the eddy current de-tumbling process, safety is realized by safety corridor constraint, and de-tumbling effect is guaranteed by desired trajectory. In the following, the design process of safety corridor and desired trajectory is elaborated according to the requirements of eddy current de-tumbling.

A. Safety corridor constraint

The safety corridor, also known as the approach corridor, is usually defined as a cone-shaped area [31]. The cone-shaped area consists of origin, central axis, and half cone angle. In autonomous rendezvous and docking (AR&D), the origin of the cone-shaped area is located at the docking interface of the target, and the central axis is parallel to the docking axis [32]. This kind of safety corridor, called ‘*Natural Safety Corridor*’ in this paper, is fixed with the target and will rotate with the rotation of the target. However, since the target is tumbling, the natural safety corridor of the target will also tumble. It increases the complexity of the controller and the fuel consumption of the chaser. Therefore, a safety corridor, called ‘*Inertial-oriented Safety Corridor*’ invariant in the inertial reference frame \mathcal{N} , is designed.

The inertial-oriented safety corridor takes the origin of the target’s body reference frame as the origin, and the angular momentum axis of the target as the central axis. It is noted that the angular momentum axis of the target is invariant without external torque. In this case, the safety corridor established in this way is inertial. However, due to the tumbling of the target, the half cone angle of the inertial-oriented safety corridor is not equal to that of the natural safety corridor. Fig.2(a) briefly illustrates three types of motion of the tumbling target, i.e., rotation (\mathbf{R}), precession (\mathbf{P}), and nutation (\mathbf{N}) [15].

Let the half cone angle of the natural safety corridor be η . The nutation angle, the angle between the x -axis of frame \mathcal{T} and angular momentum axis \mathbf{H}_t of the target, is defined as:

$$\theta = \arccos \left(\frac{\hat{\mathbf{t}}_x \cdot \mathbf{H}_t}{\|\hat{\mathbf{t}}_x\| \|\mathbf{H}_t\|} \right). \quad (12)$$

Let θ_m be the maximum value of θ . Then, as shown in Fig.2(b), the half cone angle of the inertial-oriented safety corridor α is not equal to that of the natural safety corridor η . The equation between them is

$$\alpha = \eta - \theta_m. \quad (13)$$

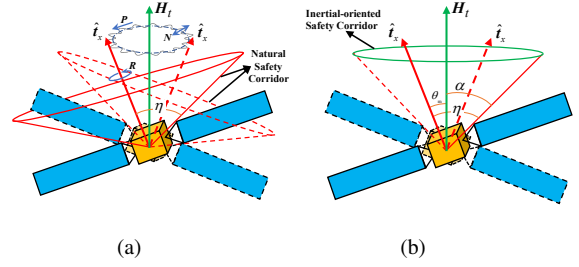


Fig. 2: (a) illustrates the tumbling motion and natural safety corridor of the target, (b) illustrates the inertial-oriented safety corridor of the target.

In addition, a linear constraint can be generated by using the rectangular cone area [16], which could reduce the computational complexity of constrained optimization problems. In this paper, the largest inscribed rectangular cone of the circular cone is taken as the safety corridor.

Define a new coordinate system, called angular momentum reference frame, as $\mathcal{H} = \{O_o, \hat{\mathbf{h}}_x, \hat{\mathbf{h}}_y, \hat{\mathbf{h}}_z\}$. The origin of \mathcal{H} is at the COG of the target, and $\hat{\mathbf{h}}_x, \hat{\mathbf{h}}_y, \hat{\mathbf{h}}_z$ define as

$$\hat{\mathbf{h}}_x = \mathbf{H}_t, \quad (14)$$

$$\hat{\mathbf{h}}_y = \hat{\mathbf{h}}_x \times \hat{\mathbf{n}}_x, \quad (15)$$

$$\hat{\mathbf{h}}_z = \hat{\mathbf{h}}_x \times \hat{\mathbf{h}}_y. \quad (16)$$

Therefore, the inertial-oriented safety corridor constraint is

$$\mathbf{A}_s \mathbf{r}^{\mathcal{H}} \leq \mathbf{0}, \quad (17)$$

where

$$\mathbf{A}_s = \begin{bmatrix} -\tan(\alpha_r) & -1 & 0 \\ -\tan(\alpha_r) & 1 & 0 \\ -\tan(\alpha_r) & 0 & -1 \\ -\tan(\alpha_r) & 0 & 1 \end{bmatrix}, \alpha_r = \arctan \left(\frac{\tan(\alpha)}{\sqrt{2}} \right). \quad (18)$$

Then, the safety corridor constraint for $\mathbf{r}^{\mathcal{N}}$ can be given by

$$\mathbb{X}_s := \{\mathbf{r}^{\mathcal{N}} | \mathbf{A}_s \mathbf{C}_{\mathcal{H}\mathcal{N}} \mathbf{r}^{\mathcal{N}} \leq \mathbf{0}\}. \quad (19)$$

Simultaneously, the upper and lower bound constraints of the system state \mathbf{x} are marked as

$$\mathbb{X}_b := \{\mathbf{x} | \mathbf{x}_{min} \leq \mathbf{x} \leq \mathbf{x}_{max}\}. \quad (20)$$

Combining the above conditions, all the constraints of the system state are

$$\mathbb{X} := \{\mathbf{x} | \mathbf{r}^{\mathcal{N}} \in \mathbb{X}_s \text{ and } \mathbf{x} \in \mathbb{X}_b\}. \quad (21)$$

REMARK 2. It can be seen from (13) that to ensure the existence of the inertial-oriented safety corridor, $\eta > \theta_m$ must be satisfied. It is satisfied for defunct satellites, e.g., Sinosat-2 [15]. For another case, e.g., Ariane-4 Upper Stage [4], the equation is not happy. If it is not satisfied, one can use the strategy of [4] or [18] to reduce the nutation angle of the target first. In addition, because the target is not free from external torque, the angular momentum reference frame proposed in this paper is not

inertial invariant. However, due to the external torque being usually small, the angular momentum of the target changes slowly. Thus, for the control and maneuver of the chaser, the target's angular momentum could be considered constant.

B. Desired trajectory

To ensure the safety of the de-tumbling process, the desired relative position is defined as follows:

$$\mathbf{r}_d^{\mathcal{N}} = r_a \frac{\mathbf{H}_t^{\mathcal{N}}}{\|\mathbf{H}_t^{\mathcal{N}}\|}, \quad (22)$$

where r_a is the radius of the spherical obstacle around center body of the target [33]. For the desired quaternion β_d , two limiting extreme configurations, parallel configuration (\parallel) and perpendicular configuration (\perp), are proposed in [4]. The parallel configuration means that the magnetic moment of the coil \mathbf{m}_{Bc} should be parallel to the relative position vector \mathbf{r}_d , that is $\mathbf{m}_{Bc} \parallel \mathbf{r}_d$, while the perpendicular configuration means $\mathbf{m}_{Bc} \perp \mathbf{r}_d$.

This paper designs the desired trajectory based on the perpendicular configuration. Combined with (9), it means $\hat{\mathbf{d}}_y$ should be perpendicular to \mathbf{r}_d . Then, the following desired attitude is given:

$$\hat{\mathbf{d}}_x^{\mathcal{N}} = \frac{\mathbf{H}_t^{\mathcal{N}}}{\|\mathbf{H}_t^{\mathcal{N}}\|}, \quad (23)$$

$$\hat{\mathbf{d}}_y^{\mathcal{N}} = \hat{\mathbf{d}}_x^{\mathcal{N}} \times \hat{\mathbf{n}}_x^{\mathcal{N}}, \quad (24)$$

$$\hat{\mathbf{d}}_z^{\mathcal{N}} = \hat{\mathbf{d}}_x^{\mathcal{N}} \times \hat{\mathbf{d}}_y^{\mathcal{N}}. \quad (25)$$

Thereby, the direction cosine matrix from \mathcal{D} frame to \mathcal{N} frame is

$$\mathbf{C}_{\mathcal{N}\mathcal{D}} = \begin{bmatrix} \hat{\mathbf{d}}_x^{\mathcal{N}} & \hat{\mathbf{d}}_y^{\mathcal{N}} & \hat{\mathbf{d}}_z^{\mathcal{N}} \end{bmatrix}, \quad (26)$$

and the desired quaternions β_d can be derived by the inverse transformations in [26].

For the continuity of the controller tracking trajectory below, the higher-order derivative of the desired trajectory is calculated by the following second-order dynamics system [34]:

$$\ddot{\mathbf{y}}_d + k_1 \dot{\mathbf{y}}_d + k_2 \mathbf{y}_d = k_2 \mathbf{y}_a(t), \quad (27)$$

where k_1 and k_2 are chosen positive constants, \mathbf{y}_a indicates the trajectory to be tracked, \mathbf{y}_d represents the desired trajectory, $\dot{\mathbf{y}}_d$ and $\ddot{\mathbf{y}}_d$ represent the first-order and second-order differential of the desired trajectory, respectively.

IV. Estimator and feedforward controller

A. Joint moving horizon estimator

The physical parameters of space debris, such as conductivity and conductor component distribution, are often unknown due to non-cooperation, collision, secondary explosion, etc. It makes that the 'Effective Magnetic Tensor' \mathbf{M}_{eff} cannot be obtained by theoretical calculation. This further results in that the de-tumbling force/torque \mathbf{p} cannot be calculated by (7). Thus, the de-tumbling force/torque needs to be estimated to guarantee

the control performance for the de-tumbling. In addition, state estimation is also necessary since there are model uncertainty and unmeasured state in the eddy current de-tumbling system [4].

The optimization-based state estimator *Moving Horizon Estimation* [19] is considered in the de-tumbling process. The estimator is suitable for multivariable nonlinear systems and can ensure that the estimated value meets the given constraints. With the improvement of computing power, this method has been applied increasingly [35]. Given this, the jMHE is developed for simultaneous state and de-tumbling force/torque estimation of eddy current de-tumbling. The joint state at time t is defined as $\mathbf{z}(t) = [\mathbf{x}(t)^\top, \mathbf{p}(t)^\top]^\top$ [36], and the corresponding joint dynamics model can be given as

$$\mathbf{z}(t) = \begin{bmatrix} \mathbf{x}(t) \\ \mathbf{p}(t) \end{bmatrix} = \begin{bmatrix} \mathbf{f}_d(\mathbf{x}(t-1), \mathbf{u}(t-1), \mathbf{p}(t-1)) \\ \mathbf{p}(t-1) + \mathbf{w}(t-1) \end{bmatrix},$$

$$= \mathbf{F}_d(\mathbf{z}(t-1), \mathbf{u}(t-1)) + \mathbf{G}_z \mathbf{w}(t-1) \quad (28)$$

$$\mathbf{y}(t) = \mathbf{C}_z \mathbf{z}(t), \quad (29)$$

where $\mathbf{f}_d(\mathbf{x}(t-1), \mathbf{u}(t-1), \mathbf{p}(t-1))$ is the discretization model of (10) by the Runge Kutta method, and $\mathbf{x}(t), \mathbf{u}(t), \mathbf{p}(t)$ are the discrete variable of $\mathbf{x}, \mathbf{u}, \mathbf{p}$ at time t . $\mathbf{w}(t)$ is the "parameter noise" for time-varying parameters, and $\mathbf{G}_z = [\mathbf{0}^\top, \mathbf{I}_{6 \times 6}^\top]^\top$, $\mathbf{C}_z = [\mathbf{C}, \mathbf{0}]$.

Naturally, the MHE optimization problem \mathcal{P}_t^{mhe} at time t can be formalized as

$$\begin{aligned} \min_{\mathbf{z}, \mathbf{w}} \quad & \Phi_M = \sum_{i=t-M}^{t-1} \left(\|\mathbf{y}_i - \mathbf{C}_z \mathbf{z}_i\|_{\mathbf{R}_{inv}}^2 + \|\mathbf{w}_i\|_{\mathbf{Q}_{inv}}^2 \right) \\ & + \Gamma(\mathbf{z}_{t-M}, \bar{\mathbf{z}}_{t-M}), \end{aligned} \quad (30)$$

subject to

$$\mathbf{z}_{i+1} = \mathbf{F}_d(\mathbf{z}_i, \mathbf{U}_i) + \mathbf{G}_z \mathbf{w}_i, i = t-M, \dots, t-1, \quad (31)$$

$$\mathbf{w}_i \in \mathbb{W}, i = t-M, \dots, t-1, \quad (32)$$

$$\mathbf{z}_i \in \mathbb{Z}, \quad i = t-M, \dots, t, \quad (33)$$

where Φ_M is the objective function of \mathcal{P}_t^{mhe} , and $M \in \mathbb{N}_+$ denotes the length of horizon window. Note that if the data horizon is not full, i.e., $t \leq M$, the full information estimator [19] is employed to estimate the joint state. $\Gamma(\mathbf{z}_{t-M}, \bar{\mathbf{z}}_{t-M}) = \|\mathbf{z}_{t-M} - \bar{\mathbf{z}}_{t-M}\|_{\bar{\mathbf{P}}_{t-M}}^2$ is the arrive cost where $\bar{\mathbf{z}}_{t-M}$ denotes the prior estimate of the joint state with a prior weighting $\bar{\mathbf{P}}_{t-M}$. $\mathbf{Z} = [\mathbf{z}_{t-M}, \dots, \mathbf{z}_t]$ is the decision variable corresponding to the joint state \mathbf{z} , and the estimated value $\hat{\mathbf{z}}_t$ is equal to the optimal solution of decision variable \mathbf{z}_t , i.e., $\hat{\mathbf{z}}_t = \mathbf{z}_t^*$. Similarly, $\mathbf{W} = [\mathbf{w}_{t-M}, \dots, \mathbf{w}_{t-1}]$ is the decision variable corresponding to parameter noise. $\mathbf{Y} = [\mathbf{y}_{t-M}, \dots, \mathbf{y}_{t-1}]$ is the measurement output from $t-M$ to $t-1$, while $\mathbf{U} = [\mathbf{u}_{t-M}, \dots, \mathbf{u}_{t-1}]$ is the control input from $t-M$ to $t-1$. \mathbb{W} and \mathbb{Z} are the constraint sets for parameter noise and joint state, respectively. \mathbf{R}_{inv} and \mathbf{Q}_{inv} are weighting matrices for parameter and measure, respectively.

REMARK 3. The time series notation of MHE usually is $\mathbf{X}_{t-i|t}, i = 1, \dots, M$. To simplify the notation, the notation $t-i$ is directly adopted in \mathcal{P}_t^{mhe} . Thus, $\bar{\mathbf{z}}_{t-M}$ means the

prior estimate at time t , which is equal to the estimated value \hat{z}_{t-M} . Meanwhile, the prior weighting \bar{P}_{t-M} is updated by Kalman Filter which is given by

$$\bar{P}_{t-M}^- = \mathbf{A}_{t-M} \bar{P}_{t-M-1} \mathbf{A}_{t-M}^\top + \mathbf{G}_z \mathbf{Q}_{inv}^{-1} \mathbf{G}_z^\top, \quad (34)$$

$$\mathbf{S}_{t-M} = \mathbf{C}_z \bar{P}_{t-M}^- \mathbf{C}_z^\top + \mathbf{R}_{inv}, \quad (35)$$

$$\mathbf{K}_{t-M} = \bar{P}_{t-M}^- \mathbf{C}_z^\top \mathbf{S}_{t-M}^{-1}, \quad (36)$$

$$\bar{P}_{t-M} = (\mathbf{I} - \mathbf{K}_{t-M} \mathbf{C}_z) \bar{P}_{t-M}^-, \quad (37)$$

where

$$\mathbf{A}_{t-M} = \left. \frac{\partial \mathbf{F}_d}{\partial \mathbf{z}} \right|_{\mathbf{z}=\hat{\mathbf{z}}_{t-M}, \mathbf{u}=\mathbf{u}_{t-M}}.$$

REMARK 4. *The Robust Asymptotic Stability (RAS) of MHE with bounded disturbances is given by [37]. However, the systems in [37] do not involve the control inputs. To deal with the combined estimation/control problem, [19] concludes that the combined MHE/MPC is RAS for nonlinear model predictive control and moving horizon estimation.*

B. Feedforward control

Let $\hat{\mathbf{x}}$ be the estimated state and $\hat{\mathbf{p}}$ be the estimated de-tumbling force/torque, and then the system dynamics model can be formulated as

$$\hat{\mathbf{x}}(t+1) = \mathbf{f}_d(\hat{\mathbf{x}}(t), \mathbf{u}(t), \hat{\mathbf{p}}(t)) + \delta(t), \quad (38)$$

where $\delta = \mathbf{f}_d(\hat{\mathbf{x}} + \mathbf{e}_x, \mathbf{u}, \hat{\mathbf{p}} + \mathbf{e}_p) - \mathbf{f}_d(\hat{\mathbf{x}}, \mathbf{u}, \hat{\mathbf{p}}) - \mathbf{e}_x^+$. The superscript $+$ indicates the value of \mathbf{e}_x at the next time. $\mathbf{e}_x = \mathbf{x} - \hat{\mathbf{x}}$ and $\mathbf{e}_p = \mathbf{p} - \hat{\mathbf{p}}$ are the estimate error for state and de-tumbling forces/torque, respectively.

Then, the estimate of de-tumbling force/torque can be compensated by a feedforward control law given as

$$\mathbf{u}(t) = \mathbf{u}_c(t) - \mathbf{B}_{inv} \hat{\mathbf{p}}(t), \quad (39)$$

where $\mathbf{u}_c(t)$ denotes the feedback control provided by the robust tracking MPC in Section V, and

$$\mathbf{B}_{inv} = \begin{bmatrix} -m_c/m_{red} \mathbf{I}_{3 \times 3} & \mathbf{0} \\ \mathbf{0} & \mathbf{I}_{3 \times 3} \end{bmatrix}.$$

Substituted (39) to the system dynamics model (38)

$$\hat{\mathbf{x}}(t+1) = \mathbf{f}_d(\hat{\mathbf{x}}(t), \mathbf{u}_c(t)) + \delta(t). \quad (40)$$

And the control constraint for the feedback control $\mathbf{u}_c(t)$ is

$$\mathbb{U}_c(t) = \{\mathbf{u}_c | \mathbf{u}_{c,min} \leq \mathbf{u}_c \leq \mathbf{u}_{c,max}\}, \quad (41)$$

where $\mathbf{u}_{c,min} = \mathbf{u}_{min} + \mathbf{B}_{inv} \hat{\mathbf{p}}(t)$, $\mathbf{u}_{c,max} = \mathbf{u}_{max} + \mathbf{B}_{inv} \hat{\mathbf{p}}(t)$. \mathbf{u}_{min} and \mathbf{u}_{max} are the upper and lower bounds of the control input \mathbf{u} .

V. Robust tracking model predictive controller

The estimator inevitably introduces an estimate error in the controller. And the controlled variable is no longer the actual state but the estimated state. In addition, unlike the setpoint problem, the controller needs to track the desired trajectory during the de-tumbling process. Therefore, we develop a robust tracking model predictive controller

(RMPC) with state-of-art methods [38], [39], [40], [41] to track the desired de-tumbling trajectory and ensure robust stability.

The optimization problem \mathcal{P}_t^{mpc} is different from the general nonlinear tracking MPC problem [38], where the predicted state $\mathbf{x}(0|t)$ is the actual state $\mathbf{x}(t)$ instead of the estimated state $\hat{\mathbf{x}}(t)$. The optimization problem \mathcal{P}_t^{mpc} is expressed as:

$$\begin{aligned} V_N(\hat{\mathbf{x}}(t), \mathbf{z}_d(\cdot|t)) &= \min_{\mathbf{u}_c(\cdot|t)} J_N(\hat{\mathbf{x}}(t), \mathbf{u}_c(\cdot|t), \mathbf{z}_d(\cdot|t)) \\ &= \min_{\mathbf{u}_c(\cdot|t)} \sum_{i=0}^{N-1} l(\hat{\mathbf{x}}(i|t), \mathbf{u}_c(i|t), \mathbf{z}_d(i|t)), \end{aligned} \quad (42)$$

subject to

$$\hat{\mathbf{x}}(0|t) = \hat{\mathbf{x}}(t), \quad (43)$$

$$\hat{\mathbf{x}}(i+1|t) = \mathbf{f}_d(\hat{\mathbf{x}}(i|t), \mathbf{u}_c(i|t)), i = 0, \dots, N-1, \quad (44)$$

$$\hat{\mathbf{x}}(i|t) \in \hat{\mathbb{X}}, i = 0, \dots, N, \quad (45)$$

$$\mathbf{u}_c(i|t) \in \hat{\mathbb{U}}_c, i = 0, \dots, N-1. \quad (46)$$

Note that the symbol $\hat{(\cdot)}$ is added only to illustrate that the controller's purpose is to force the estimated state $\hat{\mathbf{x}}$ to be robustly asymptotically stable to the desired trajectory \mathbf{x}_d . In problem \mathcal{P}_t^{mpc} , N is the prediction horizon length. And the stage cost $l(\mathbf{x}, \mathbf{u}, \mathbf{z}_d)$ is defined as

$$l(\mathbf{x}, \mathbf{u}, \mathbf{z}_d) = \|\mathbf{x} - \mathbf{x}_d\|_Q^2 + \|\mathbf{u} - \mathbf{u}_d\|_R^2, \quad (47)$$

where Q and R are the positive definite weighting matrices for state and input error, respectively. $\mathbf{z}_d = (\mathbf{x}_d, \mathbf{u}_d)$ is the desired trajectory and $\mathbf{z}_d(i|t) = \mathbf{z}_d(t+i)$. $\mathbf{u}_c(\cdot|t) = \{\mathbf{u}_c(0|t), \dots, \mathbf{u}_c(N-1|t)\}$ denotes the decision variable of control input. $\hat{\mathbb{X}}$ and $\hat{\mathbb{U}}_c$ are the state constraint and input constraint for the estimated state, respectively. Proper selection of $\hat{\mathbb{X}}$ and $\hat{\mathbb{U}}_c$ can ensure that the actual state \mathbf{x} and control input \mathbf{u}_c meet the actual state constraint \mathbb{X} and input constraint \mathbb{U}_c .

By solving the optimization problem \mathcal{P}_t^{mpc} at each sampling time t and only executing the first optimized control input $\mathbf{u}_c^*(0|t)$, we can get the MPC feedback law $\kappa(\hat{\mathbf{x}}(t))$ as follows:

$$\kappa(\hat{\mathbf{x}}(t)) = \mathbf{u}_c^*(0|t). \quad (48)$$

Then, the closed-loop system under control law $\kappa(\hat{\mathbf{x}}(t))$ is

$$\begin{aligned} \hat{\mathbf{x}}(t+1) &= \mathbf{f}_d(\hat{\mathbf{x}}(t), \kappa(\hat{\mathbf{x}}(t))) + \delta(t) \\ &= \hat{\mathbf{x}}^*(1|t) + \delta(t). \end{aligned} \quad (49)$$

REMARK 5. *From the definition of stage cost, we can know that the optimization problem \mathcal{P}_t^{mpc} is to minimize the sum of $\|\mathbf{x} - \mathbf{x}_d\|_Q^2 + \|\mathbf{u} - \mathbf{u}_d\|_R^2$ in the whole prediction horizon. Since Q and R are positive definite, the optimal objective value function $V_N(\hat{\mathbf{x}}(t), \mathbf{z}_d(\cdot|t))$ is also positive definite. Therefore, if the descent property for $V_N(\hat{\mathbf{x}}(t), \mathbf{z}_d(\cdot|t))$ can be determined, we can conclude that $V_N(\hat{\mathbf{x}}(t), \mathbf{z}_d(\cdot|t))$ is a Lyapunov function for the system. It also means that the distance between the actual trajectory (\mathbf{x}, \mathbf{u}) and the desired trajectory $(\mathbf{x}_d, \mathbf{u}_d)$ decreases, that is, the realization of trajectory tracking. In*

Section B, **Theorem 1** gives the theoretical expression of the above statement (due to the uncertainty, the descent property is robust).

A. Parameter design

In the above controller, the parameters to be designed include $\hat{\mathbb{X}}$ and $\hat{\mathbb{U}}_c$. These parameters must be carefully designed to ensure the system's iterative feasibility, stability, and constraint satisfaction.

For simplicity, the compact notation of polyhedron is used to describe the actual state constraint and input constraint as:

$$\mathbb{X} = \{\mathbf{x} | \mathbf{A}_x \mathbf{x} \leq \mathbf{b}_x\}, \mathbb{U}_c = \{\mathbf{u}_c | \mathbf{A}_u \mathbf{u}_c \leq \mathbf{b}_u\}, \quad (50)$$

where

$$\mathbf{A}_x = \begin{bmatrix} \mathbf{A}_s \mathbf{C}_{\mathcal{HN}} & | & \mathbf{0}_{4 \times 9} \\ \mathbf{I}_{12 \times 12} \\ -\mathbf{I}_{12 \times 12} \end{bmatrix}, \mathbf{b}_x = \begin{bmatrix} \mathbf{0} \\ \mathbf{x}_{max} \\ -\mathbf{x}_{min} \end{bmatrix}, \quad (51)$$

$$\mathbf{A}_u = \begin{bmatrix} \mathbf{I}_{6 \times 6} \\ -\mathbf{I}_{6 \times 6} \end{bmatrix}, \mathbf{b}_u = \begin{bmatrix} \mathbf{u}_{c,max} \\ -\mathbf{u}_{c,min} \end{bmatrix}.$$

To adopt the constraint tightening method proposed in [39], the constraint set is needed to rewrite into the normalized form, that is, $\{\mathbf{x} | \mathbf{A}_x \mathbf{x} \leq \mathbf{1}_q\}$ where $\mathbf{1}_q$ represents a column vector of one with dimension q . This form requires the polytope to contain the origin [40]. However, the origin is not the inner point of the safety constraint set (19). Therefore, the set needs to be shifted to contain the origin.

Let \mathbf{a}_s is the shifted vector that must be contained in the safety constraint set. Then, the shifted constraint set \mathbb{X}_s is

$$\begin{aligned} \mathbb{X}_s &= \{\mathbf{x} | \mathbf{A}_x (\mathbf{x} + \mathbf{a}_s) \leq \mathbf{b}_x\} \\ &= \{\mathbf{x} | \mathbf{A}_x \mathbf{x} \leq \mathbf{b}_x - \mathbf{A}_x \mathbf{a}_s\} = \{\mathbf{x} | \mathbf{A}_x \mathbf{x} \leq \mathbf{b}_{x_s}\}. \end{aligned} \quad (52)$$

Thus, we know that if $\mathbf{x} - \mathbf{a}_s \in \mathbb{X}_s$, then $\mathbf{x} \in \mathbb{X}$.

Let the shifted and normalized constraint set be

$$\mathbb{X}_s = \{\mathbf{x} | \mathbf{H}_x \mathbf{x} \leq \mathbf{1}_q\}, \mathbb{U}_s = \{\mathbf{u} | \mathbf{L}_u \mathbf{u} \leq \mathbf{1}_p\}, \quad (53)$$

where $\mathbf{H}_x = \mathbf{A}_x ./ \text{repmat}(\mathbf{b}_{x_s}, 1, 12)$, $\mathbf{L}_u = \mathbf{A}_u ./ \text{repmat}(\mathbf{b}_u, 1, 6)$. The operator $\mathbf{A} ./ \mathbf{B}$ denotes that each element of \mathbf{A} is divided by the corresponding element of \mathbf{B} , and $\text{repmat}(\mathbf{b}, i, j)$ denotes the repeat copies of \mathbf{b} into an i -by- j block arrangement.

Then, the tightened constraints can be expressed as

$$\hat{\mathbb{X}} = (1 - \epsilon_\infty) \mathbb{X}_s = \{\mathbf{x} | \mathbf{H}_x \mathbf{x} \leq (1 - \epsilon_\infty) \mathbf{1}_q\}, \quad (54)$$

$$\hat{\mathbb{U}}_c = (1 - \epsilon_\infty) \mathbb{U}_s = \{\mathbf{u} | \mathbf{L}_u \mathbf{u} \leq (1 - \epsilon_\infty) \mathbf{1}_p\}, \quad (55)$$

where $\epsilon_\infty = \frac{\epsilon}{1 - \sqrt{\rho_c}}$, $\epsilon \in \mathbb{R}_{>0}$ is a scalar tunable factor and $\rho_c \in (0, 1)$ is the exponential decay rate [39]. On the other hand, according to [41], the exponential decay rate ρ_c can be calculated by

$$\rho_c = 1 - \frac{c_{q,l}}{c_u}, \quad (56)$$

where $c_{q,l} = \lambda_{\min}(\mathbf{Q})$, $c_u = \max_{\mathbf{z}_d \in \hat{\mathbb{Z}}_d} \lambda_{\max}(\mathbf{P}_f)$. \mathbf{P}_f denotes the terminal weighting matrices obtained by

solving the discrete-time Lyapunov equation:

$$\mathbf{P}_f - (\mathbf{A}_d + \mathbf{B}_d \mathbf{K}_d)^\top \mathbf{P}_f (\mathbf{A}_d + \mathbf{B}_d \mathbf{K}_d) = \mathbf{Q}^* + \eta_c \mathbf{I}_n, \quad (57)$$

with some positive constant η_c , and

$$\mathbf{A}_d = \left. \frac{\partial \mathbf{f}_d}{\partial \mathbf{x}} \right|_{(\mathbf{x}, \mathbf{u}) = (\mathbf{x}_d, \mathbf{u}_d)}, \mathbf{B}_d = \left. \frac{\partial \mathbf{f}_d}{\partial \mathbf{u}} \right|_{(\mathbf{x}, \mathbf{u}) = (\mathbf{x}_d, \mathbf{u}_d)}. \quad (58)$$

In addition, $\mathbf{Q}^* = \mathbf{Q} + \mathbf{K}_d^\top \mathbf{R} \mathbf{K}_d$ where \mathbf{K}_d is usually obtained by solving discrete-time linear-quadratic regulator.

REMARK 6. From [39], the value of ϵ_∞ is equal to $\epsilon_k = \epsilon \frac{1 - \sqrt{\rho_c^k}}{1 - \sqrt{\rho_c}}$ as k approaches infinity, and the tightened constraints vary with k . To simplify the controller, ϵ_∞ is used to design tightening constraints. It ensures that the tightening constraints remain constant throughout the prediction.

B. System stability

For the stability guarantee of MPC, [39] gives the robust stability of MPC without terminal ingredients when stabilizing the origin, [41] gives the nominal stability of MPC without terminal ingredients when tracking the reference trajectory, and [42] gives the robust tracking stability of MPC when considering the terminal ingredients. In this paper, we consolidate the research mentioned above and provide the robust tracking stability theorem of RMPC without terminal ingredients, which is used in the de-tumbling process.

LEMMA 1. Suppose that $\mathbf{f}_d(\hat{\mathbf{x}}(t), \mathbf{u}(t))$ is twice continuously differentiable and $\hat{\mathbb{Z}}_d := \hat{\mathbb{X}} \times \hat{\mathbb{U}}_c$ is a compact set. Assume that there exists a positive definite matrix $\mathbf{P}_f(t)$ and some positive constants η_0 , such that for any $\mathbf{z}_d(t) \in \hat{\mathbb{Z}}_d$, the following matrix inequality is satisfied

$$(\mathbf{A}_d + \mathbf{B}_d \mathbf{K}_d)^\top \mathbf{P}_f^\dagger (\mathbf{A}_d + \mathbf{B}_d \mathbf{K}_d) \leq \mathbf{P}_f - \mathbf{Q}^* - \eta_0 \mathbf{I}_n, \quad (59)$$

and define

$$c_l = \min_{\mathbf{z}_d \in \hat{\mathbb{Z}}_d} \lambda_{\min}(\mathbf{P}_f), c_{q,u} = \lambda_{\max}(\mathbf{Q}),$$

$$c_{u,2} = \max_{\mathbf{z}_d \in \hat{\mathbb{Z}}_d} \lambda_{\max}(\mathbf{P}_f - \mathbf{Q}^* - \eta_0 \mathbf{I}_n),$$

$$k_u = \max_{\mathbf{z}_d \in \hat{\mathbb{Z}}_d} \|\mathbf{K}_d\|, c_{r,u} = \lambda_{\max}(\mathbf{R}).$$

The following conclusion hold as

- 1) The system $\hat{\mathbf{x}}(t+1) = \mathbf{f}_d(\hat{\mathbf{x}}(t), \mathbf{u}_c(t))$ is Locally Incrementally Stabilizable [39].
- 2) Given terminal cost $V_f(\hat{\mathbf{x}}(t), \mathbf{x}_d(t)) = \|\hat{\mathbf{x}}(t) - \mathbf{x}_d(t)\|_{\mathbf{P}_f}^2$. There exists a terminal set $\mathbb{X}_f(t) = \{\hat{\mathbf{x}}(t) | V_f(\hat{\mathbf{x}}(t), \mathbf{z}_d(t)) \leq \alpha_f\}$, such that for any $\hat{\mathbf{x}}(t) \in \mathbb{X}_f(t)$, and $\mathbf{z}_d(t) = (\mathbf{x}_d, \mathbf{u}_d) \in \hat{\mathbb{Z}}_d$, the

following properties hold :

$$V_f(\hat{\mathbf{x}}(t+1), \mathbf{z}_d(t+1)) \leq V_f(\hat{\mathbf{x}}(t), \mathbf{z}_d(t)) - l(\hat{\mathbf{x}}(t), k_f(\hat{\mathbf{x}}(t), \mathbf{z}_d(t)), \mathbf{z}_d(t)), \quad (60)$$

$$\sum_{k=0}^{\infty} l(\hat{\mathbf{x}}(t+k), k_f(\hat{\mathbf{x}}(t+k), \mathbf{z}_d(t+k)), \mathbf{z}_d(t+k)) \leq V_f(\hat{\mathbf{x}}(t), \mathbf{z}_d(t)) \leq \gamma \|\hat{\mathbf{x}}(t) - \mathbf{x}_d(t)\|_{\mathcal{Q}}^2, \quad (61)$$

$$\hat{\mathbf{x}}(t+1) \in \mathbb{X}_f(t+1), \quad (62)$$

where $\hat{\mathbf{x}}(t+1) = \mathbf{f}_d(\hat{\mathbf{x}}(t), \mathbf{u}_c(t))$, and $k_f(\hat{\mathbf{x}}(t), \mathbf{z}_d(t)) = \mathbf{u}_d(t) + \mathbf{K}_d(t)(\hat{\mathbf{x}}(t) - \mathbf{x}_d(t))$.

Proof:

Part I. The local incremental stability can be guaranteed by Lyapunov incremental stability, i.e., *Assumption 1* of [41]. *Assumption 1* of [41] can be satisfied with

$$V_\delta(x, z, v) = \|x - z\|_{\mathcal{P}_f}^2, \quad \kappa(x, z, v) = v + \mathbf{K}_d(x - z). \quad (63)$$

Let $\Delta \mathbf{x} = \hat{\mathbf{x}} - \mathbf{x}_d$, $\Delta \mathbf{u} = \kappa(\hat{\mathbf{x}}, \mathbf{x}_d, \mathbf{u}_d) = \mathbf{K}_d \Delta \mathbf{x}$. The first-order Taylor-approximation of \mathbf{f}_d around any point \mathbf{z}_d is

$$\begin{aligned} \mathbf{f}_d(\mathbf{x}_d + \Delta \mathbf{x}, \mathbf{u}_d + \Delta \mathbf{u}) \\ = \mathbf{f}_d(\mathbf{z}_d) + (\mathbf{A}_d + \mathbf{B}_d \mathbf{K}_d) \Delta \mathbf{x} + \Phi_d(\Delta \mathbf{x}, \Delta \mathbf{u}), \end{aligned}$$

where Φ_d denotes the remainder term. Twice continuous differentiability of \mathbf{f}_d in combination with the compactness of $\hat{\mathbb{Z}}$ implies that there exists T_Φ with [38]

$$\begin{aligned} \|\Phi_d(\Delta \mathbf{x}, \Delta \mathbf{u})\| &\leq T_\Phi (\|\Delta \mathbf{x}\|^2 + \|\Delta \mathbf{u}\|^2) \\ &\leq T_\Phi (1 + k_u^2) \|\Delta \mathbf{x}\|^2. \end{aligned}$$

And let the upper bound of $V_\delta(\hat{\mathbf{x}}, \mathbf{x}_d, \mathbf{u}_d)$ be given as

$$V_\delta(\hat{\mathbf{x}}, \mathbf{x}_d, \mathbf{u}_d) = \|\Delta \mathbf{x}\|_{\mathcal{P}_f}^2 \leq \delta_{loc} = c_l \left(\frac{L_\Phi}{T_\Phi (1 + k_u^2)} \right)^2,$$

where $L_\Phi = \sqrt{\frac{c_{u,2} + \eta_0}{c_u}} - \sqrt{\frac{c_{u,2}}{c_u}}$.

Thus, it can be implied that

$$\|\Phi_r(\Delta \mathbf{x}, \Delta \mathbf{u})\| \leq L_\Phi \|\Delta \mathbf{x}\|. \quad (64)$$

Then the incremental Lyapunov function satisfies

$$\begin{aligned} V_\delta(\hat{\mathbf{x}}^+, \mathbf{x}_d^+, \mathbf{u}_d^+) &= \|\hat{\mathbf{x}}^+ - \mathbf{x}_d^+\|_{\mathcal{P}_f}^2 \\ &= \|\mathbf{f}_d(\mathbf{x}_d + \Delta \mathbf{x}, \mathbf{u}_d + \Delta \mathbf{u}) - \mathbf{f}_d(\mathbf{x}_d, \mathbf{u}_d)\|_{\mathcal{P}_f}^2 \\ &= \|(\mathbf{A}_d + \mathbf{B}_d \mathbf{K}_d) \Delta \mathbf{x} + \Phi_d(\Delta \mathbf{x}, \Delta \mathbf{u})\|_{\mathcal{P}_f}^2 \\ &\leq \|(\mathbf{A}_d + \mathbf{B}_d \mathbf{K}_d) \Delta \mathbf{x}\|_{\mathcal{P}_f}^2 + \|\Phi_d(\Delta \mathbf{x}, \Delta \mathbf{u})\|_{\mathcal{P}_f}^2 \\ &\quad + 2\|\Phi_d(\Delta \mathbf{x}, \Delta \mathbf{u})\|_{\mathcal{P}_f} \|(\mathbf{A}_d + \mathbf{B}_d \mathbf{K}_d) \Delta \mathbf{x}\|_{\mathcal{P}_f}. \quad (65) \end{aligned}$$

From (59), we get

$$\begin{aligned} \|(\mathbf{A}_d + \mathbf{B}_d \mathbf{K}_d)(\hat{\mathbf{x}} - \mathbf{x}_d)\|_{\mathcal{P}_f}^2 \\ \leq \|\hat{\mathbf{x}} - \mathbf{x}_d\|_{\mathcal{P}_f}^2 - \eta_0 \|\hat{\mathbf{x}} - \mathbf{x}_d\|^2 - \|\hat{\mathbf{x}} - \mathbf{x}_d\|_{\mathcal{Q}^*}^2 \\ = V_\delta(\hat{\mathbf{x}}, \mathbf{x}_d, \mathbf{u}_d) - \eta_0 \|\Delta \mathbf{x}\|^2 - l(\hat{\mathbf{x}}, \kappa(\hat{\mathbf{x}}, \mathbf{x}_d, \mathbf{u}_d), \mathbf{z}_d). \quad (66) \end{aligned}$$

Combining with (64), the following inequation can be given as

$$\begin{aligned} \|\Phi_d(\Delta \mathbf{x}, \Delta \mathbf{u})\|_{\mathcal{P}_f}^2 \\ + 2\|\Phi_d(\Delta \mathbf{x}, \Delta \mathbf{u})\|_{\mathcal{P}_f} \|(\mathbf{A}_d + \mathbf{B}_d \mathbf{K}_d) \Delta \mathbf{x}\|_{\mathcal{P}_f} \\ \leq (L_\Phi^2 c_u + 2L_\Phi \sqrt{c_u} \sqrt{c_{u,2}}) \|\Delta \mathbf{x}\|^2 \\ = \left(c_u \left(L_\Phi + \sqrt{\frac{c_{u,2}}{c_u}} \right)^2 - c_{u,2} \right) \|\Delta \mathbf{x}\|^2 \leq \eta_0 \|\Delta \mathbf{x}\|^2. \quad (67) \end{aligned}$$

Substitute (66) and (67) to (65):

$$\begin{aligned} V_\delta(\hat{\mathbf{x}}^+, \mathbf{x}_d^+, \mathbf{u}_d^+) &\leq V_\delta(\hat{\mathbf{x}}, \mathbf{x}_d, \mathbf{u}_d) - l(\hat{\mathbf{x}}, \kappa(\hat{\mathbf{x}}, \mathbf{x}_d, \mathbf{u}_d), \mathbf{z}_d) \\ &\leq V_\delta(\hat{\mathbf{x}}, \mathbf{x}_d, \mathbf{u}_d) - \frac{c_{q,l}}{c_u} \|\Delta \mathbf{x}\|_{\mathcal{P}_f}^2 = \rho V_\delta(\hat{\mathbf{x}}, \mathbf{x}_d, \mathbf{u}_d), \end{aligned}$$

where $\rho = 1 - \frac{c_{q,l}}{c_u} \in (0, 1)$.

Part II. Let $\alpha_f = \delta_{loc}$, the (60) is set up immediately.

Let $\gamma = \frac{c_u}{c_{q,l}}$, then $V_f(\hat{\mathbf{x}}(t), \mathbf{z}_d(t)) \leq \gamma \|\hat{\mathbf{x}}(t) - \mathbf{x}_d(t)\|_{\mathcal{Q}}^2$.

Equation (61) can immediately get by $\gamma = \frac{c_u}{c_{q,l}}$ and superposition the (61) for $k = 0, \dots, \infty$. Since $l(\hat{\mathbf{x}}(t), k_f(\hat{\mathbf{x}}(t), \mathbf{z}_d(t)), \mathbf{z}_d(t)) \geq 0$, then $V_f(\hat{\mathbf{x}}(t+1), \mathbf{z}_d(t+1)) \leq V_f(\hat{\mathbf{x}}(t), \mathbf{z}_d(t)) \leq \alpha_f$. Thus $\hat{\mathbf{x}}(t+1) \in \mathbb{X}_f(t+1)$. ■

REMARK 7. For the de-tumbling process, $\mathbf{f}_d(\hat{\mathbf{x}}(t), \mathbf{u}(t))$ and $\hat{\mathbb{Z}}_d$ obviously satisfy the assumptions in lemma 1. Furthermore, since the desired trajectory designed in Sec.B is almost constant over a long time interval, it can be considered that \mathcal{P}_f^+ is equal to \mathcal{P}_f . Thus, by making $\eta_c \geq \eta_0$, (59) is satisfied.

THEOREM 1. Let lemma 1 hold. For a given bound $V_{max} \in \mathbb{R}_{>0}$, there are constants $N_0, \hat{w}, \gamma_{V_{max}}, \alpha_{w,N} \in \mathbb{R}_{>0}$. For all initial estimated state $\hat{\mathbf{x}}(0)$ satisfies $V_N(\hat{\mathbf{x}}(0), \mathbf{z}_d(\cdot|0)) \leq V_{max}$, and all disturbances $\|\mathbf{w}(t)\| \leq \hat{w}$, if the prediction horizon length $N > N_0$, the perturbed closed-loop system (49) for $t \geq 0$ satisfies

$$\begin{aligned} \|\Delta \mathbf{x}(t)\|_{\mathcal{Q}}^2 &\leq V_N(\hat{\mathbf{x}}(t), \mathbf{z}_d(\cdot|t)) \leq \gamma_{V_{max}} \|\Delta \mathbf{x}(t)\|_{\mathcal{Q}}^2, \quad (68) \\ V_N(\hat{\mathbf{x}}(t+1), \mathbf{z}_d(\cdot|t+1)) - V_N(\hat{\mathbf{x}}(t), \mathbf{z}_d(\cdot|t)) \\ &\leq 2\alpha_{w,V_{max}} (\|\mathbf{w}(t)\|) - \alpha_{w,N} l(\hat{\mathbf{x}}(t), \mathbf{u}_c(t), \mathbf{z}_d(t)). \quad (69) \end{aligned}$$

with $\alpha_{w,V_{max}}$, a class \mathcal{K} function given in [39]. In addition, the set $\mathbb{Z}_{RPI} := \{\hat{\mathbf{x}}(t) | V_N(\hat{\mathbf{x}}(t), \mathbf{z}_d(\cdot|t)) \leq V_{RPI}\}$ with $V_{RPI} := 2\alpha_{w,V_{max}}(\hat{w}) \frac{\gamma_{V_{max}}}{\alpha_{w,N}}$ is robustly stabilized.

The proof of **Theorem 1** is consistent with Theorem 8 in [39], which will not be restated here. **Theorem 1** is intended for trajectory tracking, and Theorem 8 is stable to zero, which makes the proof process of the two theorems slightly different. Readers interested in proving **Theorem 1** should keep this in mind. In addition, as discussed in [41], the theoretical proof is still quite conservative, and the prediction horizon length N required is too long. However, **Theorem 1** provides an indication of system stability, which is helpful for control system analysis and parameter adjustment.

VI. Simulation and discussion

This paper takes the Chinese Sinosat-2 satellite for simulation analysis. The satellite was launched in 2006 and failed due to a system fault. At present, it has become typical space debris. In the simulation, it is assumed that the angular velocity and attitude of Chinese Sinosat-2 are measurable. Still, its physical parameters are unknown due to long-term failure, so it is necessary to estimate the de-tumbling force/torque. The following simulation parameters are selected as Table I and Table II to demonstrate the strategy's effectiveness and conduct system simulation analysis.

TABLE I: The Physical Parameters of the Chaser and Target

| Parameter | Value | Unit |
|--------------------|--|---------------------|
| m_t | 2086.3 | kg |
| \mathbf{J}_t | diag(4513.2, 4138.1, 3282.5) | kg · m ² |
| \mathbf{M}_{eff} | $0.89 \cdot \text{diag}(5.908, 5.908, 1.951) \cdot 10^6$ | S · m ⁴ |
| R_h | 1 | m |
| N_h | 500 | — |
| I_h | 80 | A |
| m_c | 175 | kg |
| \mathbf{J}_c | diag(14.3, 17.3, 20.3) | kg · m ² |
| η | 75 | ° |
| θ_m | 10 | ° |
| r_a | 3 | m |

TABLE II: The Initial Value of the De-tumbling Phase

| Parameter | Initial Value | Unit |
|--------------|-------------------------|------|
| \mathbf{r} | [2.5; 0; 0] | m |
| \mathbf{v} | [0; 0; 0] | m/s |
| β_c | [0.3; 0.9; 0.1; 0.3] | — |
| ω_c | [0; 0; 0] | °/s |
| β_t | [1; 0; 0; 0] | — |
| ω_t | [14.364; 1.224; 3.4195] | °/s |

The sample time T_s is set to 0.1s. The parameter value about the constraints is given as: the upper and lower bounds of the system state are $\mathbf{x}_{max} = [1_9^\top, 0.21_3^\top]^\top$ and $\mathbf{x}_{min} = -\mathbf{x}_{max}$; the constraint set for parameter noise \mathbf{w} is $\mathbb{W} = \{\mathbf{w} | \mathbf{w}_{min} \leq \mathbf{w} \leq \mathbf{w}_{max}\}$ where $\mathbf{w}_{max} = [10^{-2} \mathbf{1}_3^\top, 10^{-1} \mathbf{1}_3^\top]^\top$ and $\mathbf{w}_{min} = -\mathbf{w}_{max}$; the constraint set for joint state \mathbf{z} is $\mathbb{Z} = \mathbb{X} \times \mathbb{P}$ and the constraint set for \mathbf{p} is $\mathbb{P} = \{\mathbf{p} | \mathbf{p}_{min} \leq \mathbf{p} \leq \mathbf{p}_{max}\}$ where $\mathbf{p}_{max} = [0.61_3^\top, 1_3^\top]^\top$ and $\mathbf{p}_{min} = -\mathbf{p}_{max}$. The horizon length of MHE is $M = 20$, and the covariance matrix $\mathbf{R}_{mhe} = 10^{-8} \mathbf{I}_{12}$, $\mathbf{Q}_{mhe} = 10^{-6} \mathbf{I}_{12}$. Thus, the weighting matrices $\mathbf{R}_{inv} = \mathbf{R}_{mhe}^{-1} = 10^8 \mathbf{I}_{12}$, $\mathbf{Q}_{inv} = \mathbf{Q}_{mhe}^{-1} = 10^6 \mathbf{I}_{12}$. The bound of input are $\mathbf{u}_{max} = [21_3^\top, 0.21_3^\top]^\top$ and $\mathbf{u}_{min} = -\mathbf{u}_{max}$. The prediction horizon length of MPC is $N = 10$, and weighting matrices $\mathbf{Q} = 10^8 \text{diag}(\mathbf{1}_6^\top, 20, 5, 5, \mathbf{1}_3^\top)$ and $\mathbf{R} = \mathbf{I}_6$, the shifted vector $\mathbf{a}_s = 10^{-3} \mathbf{1}_{12}$. The *CasADi* helper classes *Opti stack* [43] is applied to encode the optimization problem \mathcal{P}_t^{mhe} and \mathcal{P}_t^{mpc} , and the solver is chosen as *ipopt* [44]. The simulation results and discussion are given below.

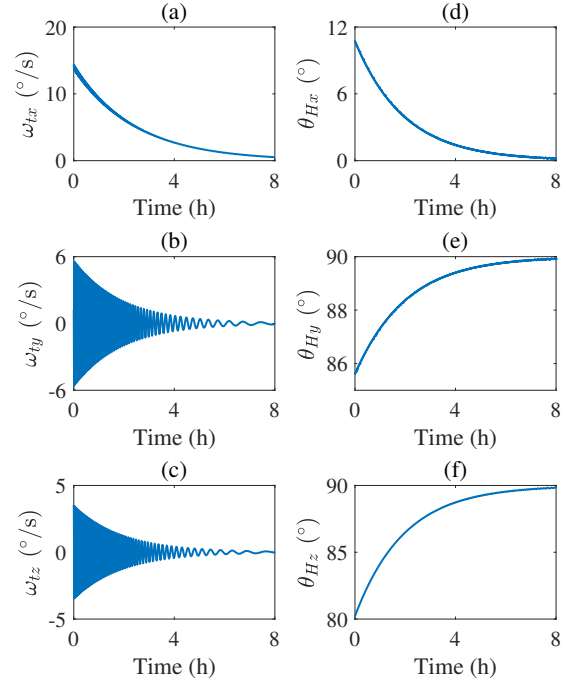


Fig. 3: Time response of target's angular velocity and angular momentum direction

Firstly, we show the de-tumbling effect of target angular velocity and angular momentum's direction angular. The angular momentum direction angle is defined as the included angle $\theta_{H,i}$ between the angular momentum axis \mathbf{H}_t and the \mathcal{N} frame's axes $\hat{\mathbf{n}}_i$, and its calculation equation is:

$$\theta_{H,i} = \arccos \left(\frac{\hat{\mathbf{n}}_i \cdot \mathbf{H}_t}{\|\hat{\mathbf{n}}_i\| \|\mathbf{H}_t\|} \right), \quad (70)$$

where $i = x, y, z$. It can be seen from the first three subgraphs in Fig.3 that the angular velocity in each axis of the target attenuated to less than 1 (°/s) within 8 hours. In contrast, it takes several days to achieve the same effect in [10]. Fig.3(b)(c) also shows that the angular velocity of the target ω_t is oscillatory decreasing. At the same time, Fig.3(d)(e)(f) demonstrates that the direction of the angular momentum of the target is monotonically changing, and the average change rate of $\theta_{H,i}$ is less than $\frac{12}{3600 \times 8} = 4.167 \times 10^{-4}$ (°/s). It also implies that the natural safety corridor will oscillate continuously with ω_t as the central axis. In contrast, the inertial-oriented safety corridor will change monotonically with the target's angular momentum as the central axis. The inertial-oriented safety corridor can be deemed constant in the control horizon since the rate of change of this angular momentum is relatively low.

From Fig.4(a), the component of desired relative position \mathbf{r}_d is less than 3 (m), which could improve the de-tumbling effect. The desired trajectory in Fig.4 has no oscillation, and the overall change is tiny. The maximum change of the desired position \mathbf{r}_d within 4 hours is less than 0.5 (m), that is, the average change

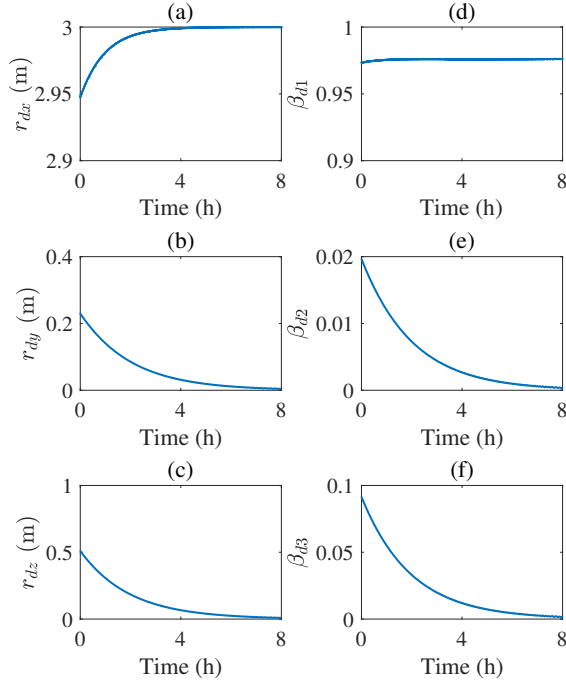


Fig. 4: Time response of desired position and attitude

rate is less than $\frac{0.5}{4 \times 3600} = 3.4722 \times 10^{-5}$ (m/s). Similarly, the average change rate of the desired attitude is less than $\frac{0.2}{4 \times 3600} = 1.3889 \times 10^{-5}$. Thus, the assumption $\mathbf{P}_f^+ = \mathbf{P}_f$ on Remark.7 is acceptable.

Next, we investigate the fuel consumption of the chaser. The equation of fuel consumption is defined as:

$$J_F = \frac{\int_0^t \|\mathbf{F}\|_2 d\tau}{I_{sp}}, \quad (71)$$

where J_F is the mass of fuel consumption, \mathbf{F} is the force vector of the chaser's thrusters, $\|\mathbf{F}\|_2$ denotes the 2-norm of \mathbf{F} , and $I_{sp} = 2000$ (m/s) denotes the specific impulse of thruster. Consistent with (24) in [45], the equation from the force vector \mathbf{F} to the control input \mathbf{u} is

$$\mathbf{u} = \mathbf{H}\mathbf{F} \quad (72)$$

where the matrix \mathbf{H} indicates the reconfiguration matrix of the thrusters relative to the chaser's body reference frame. The thruster parameters selected in this simulation are consistent with the target spacecraft parameters in [45]. The force vector \mathbf{F} is calculated directly by the pseudo-inverse scheme, i.e., $\mathbf{F} = \mathbf{H}^\dagger \mathbf{u}$, where \mathbf{H}^\dagger denotes the pseudo-inverse of \mathbf{H} . The fuel consumption of the chaser is shown in Fig.5(a).

As shown in Fig.5(a), the fuel consumption of the whole de-tumbling does not exceed 3.5 (kg), which is acceptable for space missions. In addition, since the pseudo-inverse scheme used in this simulation is not optimal, the fuel consumption can be further reduced by adopting the scheme [46].

In addition, Fig.5(b) shows the CPU time used to solve the optimization problem of RMPC \mathcal{P}_t^{mpc} at each sampling time in the first 40 (s). The simulation runs on

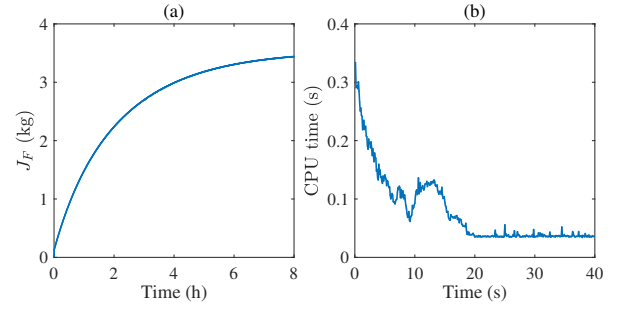


Fig. 5: Time response of fuel consumption and CPU time

a Dell laptop of Windows 10 with Intel(R) Core(TM) i7-8750H CPU @2.20GHz @2.21GHz. Due to the error between the actual trajectory and the desired trajectory, the solver needs to spend more time looking for an optimal solution in the early stage (between 0 (s) and 20 (s)), which results in longer CPU time. However, as the trajectory gradually approaches the desired trajectory, the CPU time gradually decreases and remains below 0.04 (s).

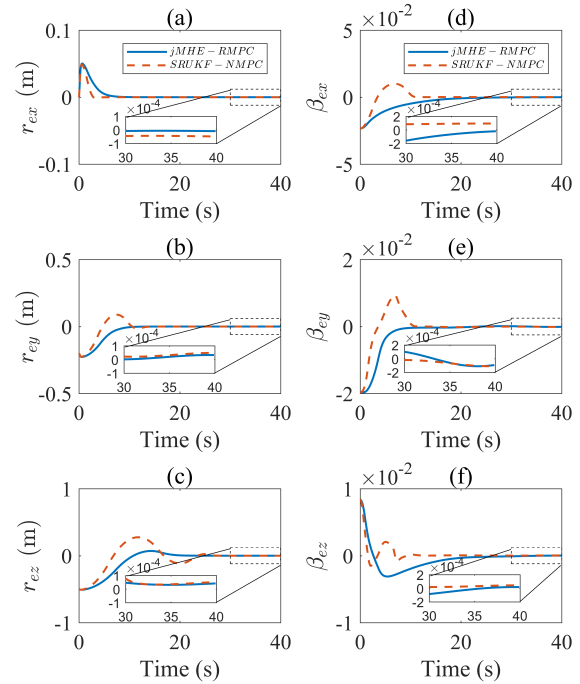


Fig. 6: Time response of position and attitude error

Next, the performance of the proposed scheme and its comparison with the state-of-art schemes will be discussed in detail. To illustrate the effectiveness of the comparison, we mainly investigate the other model predictive control and nonlinear Bayesian estimation schemes, such as nonlinear nominal model predictive control (NMPC) [21] and Square-Root Unscented Kalman Filter (SR-

UKF) [24]². These schemes can choose the same tunable parameters as the scheme proposed in this paper.

Fig.6 shows the time response of the position error and the attitude error in the first 40 (s) by jMHE-RMPC and SRUKF-NMPC. Since the subsequent processes are stable tracking processes and do not indicate the controller's performance, they are not fully displayed. As shown in Fig.6, the chaser's position and attitude converge to the desired value within tracking errors of $1 \times 10^{-4} \times [-\mathbf{1}_{12}, \mathbf{1}_{12}]$ for position and $2 \times 10^{-4} \times [-\mathbf{1}_{12}, \mathbf{1}_{12}]$ for attitude.

TABLE III: The stability parameters and their values of jMHE-RMPC and SRUKF-NMPC

| Scheme | State | Rise Time (s) | Peak Time (s) | Settling Time (s) | Percent Overshoot |
|------------|--------------|---------------|---------------|-------------------|-------------------|
| jMHE-RMPC | r_{ex} | 15.5 | 20.4 | 5.3 | 0.025% |
| | r_{ey} | 17.2 | 20.5 | 8.9 | 0.018% |
| | r_{ez} | 10.8 | 14.3 | 17.6 | 14.135% |
| | β_{ex} | 28.5 | / | 18.1 | / |
| | β_{ey} | 24.1 | 28.3 | 7.3 | 0.597% |
| | β_{ez} | 2.7 | 5.4 | 18.6 | 37.05% |
| SRUKF-NMPC | r_{ex} | 2.3 | 2.6 | 1.9 | 2.458% |
| | r_{ey} | 4.7 | 7.5 | 12.5 | 44.188% |
| | r_{ez} | 6.9 | 11.7 | 22.8 | 55.106% |
| | β_{ex} | 3.5 | 7.0 | 10.2 | 42.732% |
| | β_{ey} | 3.6 | 6.9 | 9.9 | 47.642% |
| | β_{ez} | 1.6 | 2.1 | 8.0 | 18.145% |

Table III shows the stability parameters and their values of jMHE-RMPC and SRUKF-NMPC. Note that there is an infeasible solution to the optimization problem of SRUKF-NMPC under the current control constraint $\mathbb{U} := \{\mathbf{u} | \mathbf{u}_{min} \leq \mathbf{u} \leq \mathbf{u}_{max}\}$. Therefore, we have to relax the control constraint of SRUKF-NMPC to $2\mathbb{U}$, also obtained from the control input comparison curves in Fig.7. Table III indicates that SRUKF-NMPC has a better rapid response than jMHE-MPC, i.e., shorter rise time and peak time, but worse response matching similarity in most cases, i.e., greater overshoot. However, as mentioned above, SRUKF-NMPC needs relaxed control constraint to ensure the scheme's implementation.

Meanwhile, Fig.7 indicates the time response of control input of RMPC(\mathbf{u}), RMPC(\mathbf{u}_c), and NMPC. Due to the existence of feedforward control, the upper bound of \mathbf{u}_c changes in the whole control process. Still, the actual control input \mathbf{u} strictly meets the control constraint. After the chaser reaches the desired trajectory, \mathbf{u}_c becomes very small, and the subsequent value of \mathbf{u} is mainly used to compensate for de-tumbling force and torque. In addition, Fig.7 also shows that the control constraints of NMPC are relaxed.

²In fact, Feedback Linearization Model Predictive Control (FL-MPC) [18], Contractive Model Predictive Control (CNTMPC) [25], EKF and UKF [23] have also been considered. However, they all have some disastrous problems with the same parameters of this paper, such as infeasible optimization problem (FL-MPC, CNTMPC), excessive estimation error (EKF), and non-positive definite covariance matrix (UKF).

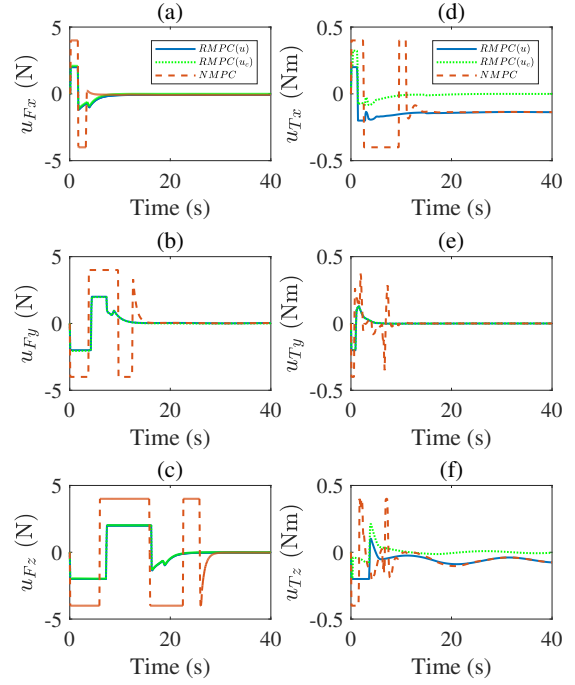


Fig. 7: Time response of control force and torque

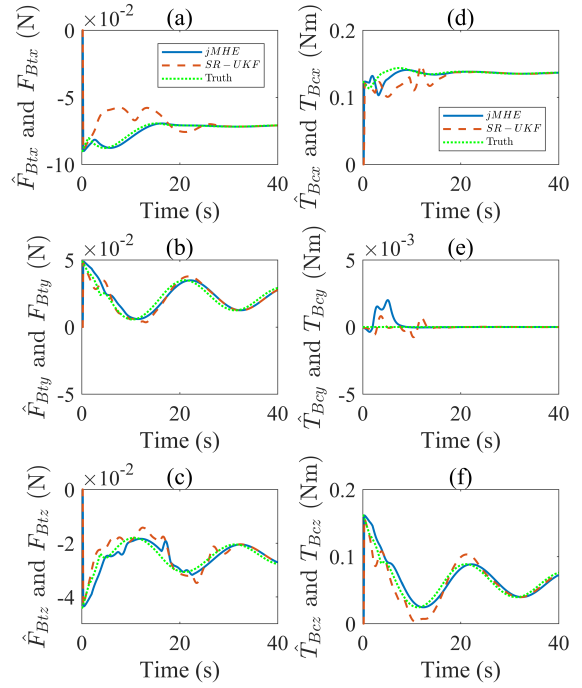


Fig. 8: Time response of true value and estimated value

Fig.8 shows the true and estimated value of de-tumbling force/torque. The initial estimation guess of unknown de-tumbling force and torque is $\mathbf{0}$, which means no prior information is used in the estimator. It also leads to a substantial estimation error at the initial time. However, the estimator quickly converges to the true value and continuously tracks it, although the true value is time-varying. For comparison, UKF can also converge near the true value, but with slower convergence and

greater oscillation, that is, SRUKF is more sensitive and unstable than jMHE under the same initial covariance. Fig.9 points out that the final estimation error of estimated force is $0.01 \times [-1_3, 1_3]$ (N), and the final estimation error of estimated torque is $0.01 \times [-1_3, 1_3]$ (N · m) for both estimators. In addition, there is no overshoot in the estimated value, which ensures the feasibility of the model predictive controller.

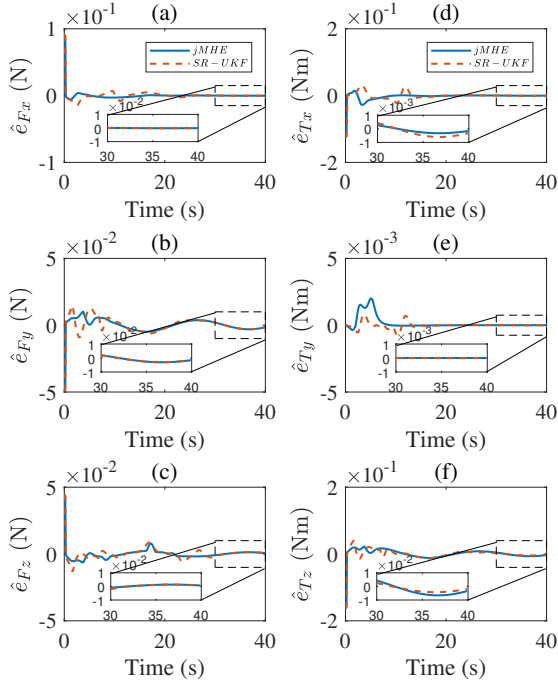


Fig. 9: Time response of the estimation error

VII. Conclusion

Robust output-feedback tracking control for proximity eddy current de-tumbling is studied with safety corridor constraint, input saturation, and model uncertainty. Considering the tumbling motion of the debris and the collision avoidance requirements of the chaser, we propose an inertial-oriented safety corridor, which essentially avoids the time-varying problem of the natural safety corridor and reduces the complexity of eddy current de-tumbling. For the problem of robust output-feedback control under safety constraint and input saturation, we propose a jMHE-RMPC scheme to estimate and compensate for the model uncertainty and realize tracking control of the eddy current de-tumbling without velocity and angular velocity measurement. Finally, the effectiveness of the proposed schemes is illustrated by taking the Chinese Sinosat-2 satellite as an example. By comparing with the state-of-art methods, we draw the following conclusions:

- 1) The safety corridor and desired trajectory designed in this paper realize the eddy current de-tumbling within the acceptable fuel consumption and reduce the chaser's maneuvering frequency;

- 2) The developed estimator can estimate the state and de-tumbling force/torque at the same time, and the estimate values are stable and high accurate;
- 3) The proposed jMHE-RMPC scheme has robust stability and constraint satisfaction under time-varying model uncertainty and without velocity-level information.

Due to the inevitability of sensor noise, future research will focus on de-tumbling trajectory planning with the target's angular velocity measurement noise and robust stability estimation and control with output measurement noise.

REFERENCES

- [1] E. S. A. (ESA) Space Debris by the numbers. (2022, Jan 05). [Online]. Available: https://www.esa.int/Safety_Security/Space_Debris/Space_debris_by_the_numbers
- [2] P. Chrystal, D. McKnight, P. L. Meredith, J. Schmidt, M. Fok, and C. Wetton *Space debris: On collision course for insurers?*, Swiss Reinsurance Company Ltd, 2011.
- [3] J. Šilha, J.-N. Pittet, M. Hamara, and T. Schildknecht Apparent rotation properties of space debris extracted from photometric measurements *Advances in Space Research*, vol. 61, no. 3, pp. 844–861, Feb 2018. [Online]. Available: <https://linkinghub.elsevier.com/retrieve/pii/S027311771730786X>
- [4] N. O. Gómez Eddy currents applied to space debris objects Ph.D. dissertation, University of Southampton, 2017.
- [5] Y.-Q. Liu, Z.-W. Yu, X.-F. Liu, and G.-P. Cai Active detumbling technology for high dynamic non-cooperative space targets *Multibody System Dynamics*, vol. 47, no. 1, pp. 21–41, 2019.
- [6] D. Han, P. Huang, X. Liu, and Y. Yang Combined spacecraft stabilization control after multiple impacts during the capture of a tumbling target by a space robot *Acta Astronautica*, vol. 176, pp. 24–32, 2020.
- [7] F. Casale, H. Schaub, and J. Douglas Biggs Lyapunov optimal touchless electrostatic detumbling of space debris in geo using a surface multisphere model *Journal of Spacecraft and Rockets*, vol. 58, no. 3, pp. 764–778, 2021.
- [8] Y. Nakajima, H. Tani, T. Yamamoto, N. Murakami, S. Mitani, and K. Yamanaka Contactless space debris detumbling: A database approach based on computational fluid dynamics *Journal of Guidance, Control, and Dynamics*, vol. 41, no. 9, pp. 1906–1918, 2018.
- [9] F. Sugai, S. Abiko, T. Tsujita, X. Jiang, and M. Uchiyama Detumbling an uncontrolled satellite with contactless force by using an eddy current brake In *2013 IEEE/RSJ International Conference on Intelligent Robots and Systems*, 2013, pp. 783–788.
- [10] N. O. Gómez and S. J. Walker Guidance, navigation, and control for the eddy brake method *Journal of Guidance, Control, and Dynamics*, vol. 40, no. 1, pp. 52–68, 2017.
- [11] P. K. Kadaba and K. Naishadham Feasibility of noncontacting electromagnetic despinning of a satellite by inducing eddy currents in its skin. i. analytical considerations *IEEE transactions on magnetics*, vol. 31, no. 4, pp. 2471–2477, 1995.

- [12] N. O. Gómez and S. J. Walker
Eddy currents applied to de-tumbling of space debris: Analysis and validation of approximate proposed methods
Acta Astronautica, vol. 114, pp. 34–53, Sept. 2015.
- [13] Q. Li, S. Song, C. Sun, Q. Gou, and Z. Niu
Robust output-feedback control for spacecraft proximity operations with forbidden zone
IEEE Transactions on Aerospace and Electronic Systems, vol. 58, no. 1, pp. 96–107, Feb 2022. [Online]. Available: <https://ieeexplore.ieee.org/document/9525151/>
- [14] C. Zagaris, H. Park, J. Virgili-Llop, R. Zappulla, M. Romano, and I. Kolmanovsky
Model predictive control of spacecraft relative motion with convexified keep-out-zone constraints
Journal of Guidance, Control, and Dynamics, vol. 41, no. 9, pp. 2054–2062, 2018.
- [15] W. Xu, L. Yan, Z. Hu, and B. Liang
Area-oriented coordinated trajectory planning of dual-arm space robot for capturing a tumbling target
Chinese Journal of Aeronautics, vol. 32, no. 9, pp. 2151–2163, 2019.
- [16] P. Li and Z. H. Zhu
Model predictive control for spacecraft rendezvous in elliptical orbit
Acta Astronautica, vol. 146, pp. 339–348, 2018.
- [17] X. Shao and Q. Hu
Immersion and invariance adaptive pose control for spacecraft proximity operations under kinematic and dynamic constraints
IEEE Transactions on Aerospace and Electronic Systems, vol. 57, no. 4, pp. 2183–2200, Aug 2021. [Online]. Available: <https://ieeexplore.ieee.org/document/9329140/>
- [18] X. Liu, H. Chang, and P. Huang
Eddy current de-tumbling large geostationary debris based on feedback linearization model predictive control
Aerospace Science and Technology, vol. 112, p. 106641, 2021.
- [19] J. B. Rawlings, D. Q. Mayne, and M. Diehl
Model predictive control: theory, computation, and design. Nob Hill Publishing Madison, WI, 2017, vol. 2.
- [20] Z. Lu, N. Wang, and C. Yang
A novel iterative identification based on the optimised topology for common state monitoring in wireless sensor networks
International Journal of Systems Science, vol. 0, no. 0, pp. 1–15, 2021.
- [21] B. Wang, Z. Meng, C. Jia, and P. Huang
Reel-based tension control of tethered space robots
IEEE transactions on aerospace and electronic systems, vol. 56, no. 4, pp. 3028–3043, 2019.
- [22] P. Kühn, M. Diehl, T. Kraus, J. P. Schlöder, and H. G. Bock
A real-time algorithm for moving horizon state and parameter estimation
Computers & chemical engineering, vol. 35, no. 1, pp. 71–83, 2011.
- [23] H. Fang, N. Tian, Y. Wang, M. Zhou, and M. A. Haile
Nonlinear bayesian estimation: From kalman filtering to a broader horizon
IEEE/CAA Journal of Automatica Sinica, vol. 5, no. 2, pp. 401–417, 2018.
- [24] G. Fang, Y. Zhang, P. Huang, and F. Zhang
State estimation of a three-inline space tethered system with geometric constraints
Advances in Space Research, vol. 69, no. 3, pp. 1550–1563, Feb 2022. [Online]. Available: <https://linkinghub.elsevier.com/retrieve/pii/S0273117721008528>
- [25] S. de Oliveira Kothare and M. Morari
Contractive model predictive control for constrained nonlinear systems
IEEE Transactions on Automatic Control, vol. 45, no. 6, pp. 1053–1071, Jun 2000. [Online]. Available: <http://ieeexplore.ieee.org/document/863592/>
- [26] J. L. Junkins and H. Schaub
Analytical mechanics of space systems. American Institute of Aeronautics and Astronautics, 2009, pp. 154,104–105.
- [27] Y. Nakajima, H. Tani, T. Yamamoto, N. Murakami, S. Mitani, and K. Yamanaka
Contactless space debris detumbling: a database approach based on computational fluid dynamics
Journal of Guidance, Control, and Dynamics, vol. 41, no. 9, pp. 1906–1918, 2018.
- [28] Y. Gao, D. Li, and S. S. Ge
Time-synchronized tracking control for 6-dof spacecraft in rendezvous and docking
IEEE Transactions on Aerospace and Electronic Systems, 2021.
- [29] B. Jiang, Q. Hu, and M. I. Friswell
Fixed-time rendezvous control of spacecraft with a tumbling target under loss of actuator effectiveness
IEEE Transactions on Aerospace and Electronic Systems, vol. 52, no. 4, pp. 1576–1586, Aug 2016. [Online]. Available: <http://ieeexplore.ieee.org/document/7738339/>
- [30] H. Dong and X. Yang
Finite-time prescribed performance control for space circumnavigation mission with input constraints and measurement uncertainties
IEEE Transactions on Aerospace and Electronic Systems, pp. 1–1, 2022.
- [31] W. Fehse
Automated rendezvous and docking of spacecraft. Cambridge university press, 2003, vol. 16.
- [32] R. Zappulla, H. Park, J. Virgili-Llop, and M. Romano
Real-time autonomous spacecraft proximity maneuvers and docking using an adaptive artificial potential field approach
IEEE Transactions on Control Systems Technology, vol. 27, no. 6, pp. 2598–2605, 2019.
- [33] D. Zhou, Y. Zhang, and S. Li
Receding horizon guidance and control using sequential convex programming for spacecraft 6-dof close proximity
Aerospace Science and Technology, vol. 87, pp. 459–477, 2019.
- [34] J.-J. E. Slotine and W. Li
Applied nonlinear control. Prentice hall Englewood Cliffs, NJ, 1991, vol. 199, no. 1, p. 195.
- [35] B. Wang, Z. Ma, S. Lai, L. Zhao, and T. H. Lee
Differentiable moving horizon estimation for robust flight control
In *2021 60th IEEE Conference on Decision and Control (CDC)*. IEEE, 2021, pp. 3563–3568.
- [36] E. Wan and R. Van Der Merwe
The unscented kalman filter for nonlinear estimation
In *Proceedings of the IEEE 2000 Adaptive Systems for Signal Processing, Communications, and Control Symposium (Cat. No.00EX373)*, 2000, pp. 153–158.
- [37] M. A. Müller
Nonlinear moving horizon estimation in the presence of bounded disturbances
Automatica, vol. 79, pp. 306–314, 2017.
- [38] J. Kohler, M. A. Muller, and F. Allgower
A nonlinear model predictive control framework using reference generic terminal ingredients
IEEE Transactions on Automatic Control, vol. 65, no. 8, pp. 3576–3583, Aug 2020. [Online]. Available: <https://ieeexplore.ieee.org/document/8882372/>
- [39] J. Köhler, M. A. Müller, and F. Allgöwer
A novel constraint tightening approach for nonlinear robust model predictive control
In *2018 Annual American Control Conference (ACC)*. IEEE, 2018, pp. 728–734.
- [40] F. Borrelli, A. Bemporad, and M. Morari
Predictive Control for Linear and Hybrid Systems, 1st ed. Cambridge University Press, Jun 2017.
- [41] J. Kohler, M. A. Muller, and F. Allgower

Nonlinear reference tracking: An economic model predictive control perspective

IEEE Transactions on Automatic Control, vol. 64, no. 1, pp. 254–269, Jan 2019. [Online]. Available: <https://ieeexplore.ieee.org/document/8278210/>

- [42] J. Köhler, M. A. Müller, and F. Allgöwer
A nonlinear model predictive control framework using reference generic terminal ingredients – extended version
arXiv preprint arXiv:1909.12765, 2019.
- [43] J. A. E. Andersson, J. Gillis, G. Horn, J. B. Rawlings, and M. Diehl
CasADi – A software framework for nonlinear optimization and optimal control
Mathematical Programming Computation, vol. 11, no. 1, pp. 1–36, 2019.
- [44] A. Wächter and L. T. Biegler
On the implementation of an interior-point filter line-search algorithm for large-scale nonlinear programming
Mathematical programming, vol. 106, no. 1, pp. 25–57, 2006.
- [45] P. Huang, Y. Lu, M. Wang, Z. Meng, Y. Zhang, and F. Zhang
Postcapture attitude takeover control of a partially failed spacecraft with parametric uncertainties
IEEE Transactions on Automation Science and Engineering, vol. 16, no. 2, pp. 919–930, Apr 2019. [Online]. Available: <https://ieeexplore.ieee.org/document/8520805/>
- [46] X. Lang and A. de Ruiter
Distributed optimal control allocation for 6-dof spacecraft with redundant thrusters
Aerospace Science and Technology, vol. 118, p. 106971, 2021.



Zhenyu Lu (Member, IEEE) received the Ph.D degree in Northwestern Polytechnical University, Xi’an, China in 2019. He is currently working as a senior research fellow in Bristol Robotic Laboratory & University of the West of England, Bristol. His research interests include teleoperation, human–robotics interaction and intelligent learning method.



Xiyao Liu (Student Member, IEEE) received the B.S. degree from Southwest Jiaotong University, Chengdu, China, in 2016. He is currently working toward the Ph.D. degree in navigation, guidance and control at the School of Astronautics, Northwestern Polytechnical University, Xi’an, China. His research focuses on model predictive control, data driven control, moving horizon estimation, and eddy current detumbling.



Haitao Chang (Member, IEEE) received B.S., M.S. and Ph.D. in navigation, guidance and control from Northwestern Polytechnical University, Xi’an China in 2010, 2013 and 2018 respectively. He is currently an assistant research professor with the School of Astronautics, Northwestern Polytechnical University. His research interests include space robot and control, space teleoperation, and space debris removal, etc.



Panfeng Huang (Senior Member, IEEE) received the B.S. degree in test and measurement technology and the M.S. degree in navigation guidance and control from Northwestern Polytechnical University, Xi’an, China, in 1998 and 2001, respectively, and the Ph.D. degree in automation and robotics from The Chinese University of Hong Kong, Hong Kong, in 2005. He is currently a Professor with the School of Astronautics, Northwestern Polytechnical University,

and the National Key Laboratory of Aerospace Flight Dynamics, and the Director of the Research Center for Intelligent Robotics, Northwestern Polytechnical University. His current research interests include tethered space robotics, intelligent control, machine vision, and space debris removal.